

## Incompressible SPH simulation of wave breaking and overtopping with turbulence modelling

Songdong Shao<sup>1,2,\*†‡</sup>

<sup>1</sup>*School of Mathematics and Statistics, University of Plymouth, Drake Circus, Plymouth PL4 8AA, U.K.*

<sup>2</sup>*School of Engineering, University of Plymouth, Drake Circus, Plymouth PL4 8AA, U.K.*

### SUMMARY

In this paper a truly incompressible version of the smoothed particle hydrodynamics (SPH) method is presented to investigate the surface wave overtopping. SPH is a pure Lagrangian approach which can handle large deformations of the free surface with high accuracy. The governing equations are solved based on the SPH particle interaction models and the incompressible algorithm of pressure projection is implemented by enforcing the constant particle density. The two-equation  $k$ – $\varepsilon$  model is an effective way of dealing with the turbulence and vortices during wave breaking and overtopping and it is coupled with the incompressible SPH numerical scheme. The SPH model is employed to reproduce the experiment and computations of wave overtopping of a sloping sea wall. The computations are validated against the experimental and numerical data found in the literatures and good agreement is observed. Besides, the convergence behaviour of the numerical scheme and the effects of particle spacing refinement and turbulence modelling on the simulation results are also investigated in further detail. The sensitivity of the computed wave breaking and overtopping on these issues is discussed and clarified. Copyright © 2005 John Wiley & Sons, Ltd.

KEY WORDS: SPH; incompressible scheme; wave overtopping; wave breaking; turbulence;  $k$ – $\varepsilon$  model

### 1. INTRODUCTION

The design of breakwaters that allow overtopping has many benefits and is being given great attention in practice. Wave overtopping is a violent natural phenomenon which can cause the

---

\*Correspondence to: Songdong Shao, School of Mathematics and Statistics, University of Plymouth, Drake Circus, Plymouth PL4 8AA, U.K.

†E-mail: shao@coast.kuciv.kyoto-u.ac.jp, songdong.shao@plymouth.ac.uk

‡Former Postdoctoral Fellow of Japan Society for the Promotion of Science (JSPS). Waterfront Environmental Engineering, Department of Urban and Environmental Engineering, Kyoto University, Kyoto 606-8501, Japan. Currently, Joint Research Fellow, School of Mathematics and Statistics and School of Engineering, University of Plymouth, U.K.

Contract/grant sponsor: Japan Society for the Promotion of Science (JSPS)

Contract/grant sponsor: University of Plymouth

*Received 6 May 2005*

*Revised 4 July 2005*

*Accepted 17 July 2005*

failure of structures and damage to the properties and life. Previous investigations on the wave overtopping mainly focused on the empirical formula derived from the laboratory experiments or field observations. Besides, lots of analytical work has also been done in this regard. However, there are strong limitations in putting these results into practice, since they rely heavily on a particular site and configuration. Therefore, there is a great interest in developing techniques which can predict the wave overtopping accurately and remain applicable over a whole range of structure geometry, water level and wave condition. Numerical models that solve the equations of fluid flow appear to provide just such an approach. Nonetheless, the fluid flows in the breaking and overtopping surface waves are highly complex, involving the interactions between the wave and structure, the strong turbulence and eddy vortices.

Numerous progresses have been made in the numerical simulations of these types of flows. For example, Liu *et al.* [1] presented a Reynolds-averaged Navier–Stokes (RANS) model for simulating the breaking waves overtopping of a porous structure, in which an improved  $k-\epsilon$  model and VOF surface tracking scheme were coupled with their solver. Hu *et al.* [2], Shiach *et al.* [3] and Stansby and Feng [4] employed different forms of the shallow water equations (SWE) to study the surface waves overtopping of a structure using the finite volume method. Numerical studies of wave overtopping of simple sea walls using a RANS approach were also reported by Soliman [5], Soliman and Reeve [6] and Garcia *et al.* [7]. Li *et al.* [8] carried out a detailed investigation into the wave overtopping of a sea wall by solving the N–S equations coupled with VOF surface tracking scheme and LES modelling technique. They also further investigated the effects of grid spacing refinement, Reynolds number, surface tension and turbulence modelling on the overtopping wave simulations.

Since the wave overtopping accompanied by breaking is an abrupt and large deformation of the water surfaces, the numerical models based on the traditional Eulerian grid methods, which discretize the governing equations using a fixed computational grid, bring the problem of numerical diffusion on the free surface. Numerical diffusion smoothes the shape of water surface and sometimes dominates the computation. As a result, another kind of numerical model completely different from the Eulerian approach, i.e. the particle model, has attracted considerable attention recently. In the particle method, the governing equations are discretized and solved using individual particles distributed within the computational domain and there is no grid needed. For instance, the moving particle semi-implicit (MPS) method initially put forward by Koshizuka *et al.* [9] is a robust particle approach. It has been successfully applied to wave breaking and overtopping at an upright sea wall by Hayashi *et al.* [10]. Another very powerful particle modelling approach, which is employed in the present paper, is called the smoothed particle hydrodynamics (SPH) method. SPH was originally developed for the study of astrophysics [11, 12] and recently employed to study the wave overtopping over the structure by Gomez-Gesteira *et al.* [13]. In their simulations of incompressible flows using the SPH, the incompressibility was realized through a stiff equation of state so that the fluid was considered to be slightly compressible. This approach is denoted as the weakly compressible SPH, since a large sound speed has to be introduced into the pressure equation to ensure the numerical stability. Based on the semi-implicit algorithm of the MPS method [9], a truly incompressible version of the SPH [14] has been proposed, in which the free surfaces were identified and tracked by particles without numerical diffusion. The key difference between the original weakly compressible SPH [11, 12] and the incompressible SPH [14] lies in that the former calculates the pressure using an equation of state, while the latter employs a

strict incompressible SPH formulation, in which the pressure is not an explicit thermodynamic variable but obtained implicitly through solving a pressure Poisson equation derived from the mass and momentum equations. In this sense, it is also very similar to the pressure projection method widely used in a grid method and the projection SPH of Cummins and Rudman [15].

Turbulence modelling is another key issue to be addressed in the study of breaking and overtopping waves. For the non-breaking waves, the potential flow theory can be used with enough accuracy. While for the breaking waves, the flow becomes highly rotational and complicated, thus necessitating the implementation of more sophisticated descriptions of wave dynamics. At the current stage, direct numerical simulation (DNS) is still impossible for the high Reynolds number flows in large computational domains. Large eddy simulation (LES) has been put forward to balance the computational accuracy and efficiency. However, LES still needs a very fine grid and this requirement cannot easily be achieved in practice. On the other hand, the RANS equations coupled with different turbulent closure models have enjoyed great success in a wide variety of practical fields. Turbulent stresses in the RANS equations can be closed using any of the turbulence models. Among the existing turbulent closure schemes, the two-equation  $k-\varepsilon$  model might be the most popular one which has undergone numerous tests. For example, Lin and Liu [16] and Bradford [17] successfully employed the  $k-\varepsilon$  model to investigate the surf zone wave breaking.

Until now it seems that no specific turbulence model has ever been designed for the SPH approach. Monaghan [18] put forward the conception of compressible turbulence in SPH. This SPH alpha model is an extension of the original XSPH algorithm [12], which aimed to reduce the particle disorder at short length scales and thus retain the constants of motion. A hydrodynamic turbulence modelling based on the eddy viscosity model was used by Violeau *et al.* [19] in the SPH simulations for a Poiseuille turbulence flow. Recently, good progresses have been achieved in coupling the advanced turbulence models with the SPH conception. For instance, Shao and Gotoh [20] used a 2-D sub-particle scale (SPS) turbulence model to simulate a dam break and wave breaking on the beach using the MPS and SPH solvers. This LES-SPS turbulence model, which was derived from the LES formulation, was initially put forward by Gotoh *et al.* [21] in the hydraulic applications. In the latest work of Shao [22], a commonly used two-equation  $k-\varepsilon$  model was coupled with the incompressible SPH method to investigate the spilling and plunging waves breaking over a slope. The numerical predictions of surf zone properties are in good agreement with the experimental and numerical data found from the literatures. In the present paper, we use the numerical model of Shao [22] to investigate wave breaking and overtopping of a sea wall, since this version of the model is a natural combination of the SPH philosophy with a well-known turbulence modelling approach in the hydrodynamic fields.

The paper is organized in the following ways. First, the governing equations and two-equation  $k-\varepsilon$  turbulence model for the incompressible SPH approach are presented. Second, the equation solution processes are formulated, in which a semi-implicit algorithm to compute the pressure employing an incompressible numerical scheme is proposed. Third, the classical SPH conceptions and formulations of Monaghan [12] are reviewed. Then the boundary and free surface conditions which are essential for the SPH computations are discussed. Finally, the numerical model is applied to simulate the wave overtopping of a sloping sea wall following the work of Li *et al.* [8]. The convergence behaviour of the numerical model, the effects of particle spacing refinement and turbulence modelling on the simulations of overtopping waves are also further investigated based on different SPH runs.

## 2. GOVERNING EQUATIONS AND TURBULENCE MODEL

### 2.1. Governing equations

Employing the SPH particle approach, the governing mass and momentum equations for a turbulent flow are presented in the following Lagrangian form:

$$\frac{1}{\rho} \frac{D\rho}{Dt} + \nabla \cdot \mathbf{u} = 0 \quad (1)$$

$$\frac{D\mathbf{u}}{Dt} = -\frac{1}{\rho} \nabla P + \mathbf{g} + \nu_0 \nabla^2 \mathbf{u} + \frac{1}{\rho} \nabla \cdot \vec{\tau} \quad (2)$$

where  $\rho$  is the density,  $t$  the time,  $\mathbf{u}$  the velocity,  $P$  the pressure,  $\mathbf{g}$  the gravitational acceleration,  $\nu_0$  the kinematic viscosity of laminar flow, and  $\vec{\tau}$  the turbulent Reynolds stresses. The mass conservation equation (1) is written in the form of a compressible flow using a full derivative. The purpose is to impose the incompressibility by setting  $D\rho/Dt = 0$  on fluid particles during the semi-implicit incompressible SPH computations.

### 2.2. Two-equation $k$ - $\varepsilon$ turbulence model

The  $k$ - $\varepsilon$  model has enjoyed great popularity in the numerical hydrodynamics. It is an important turbulent closure model on the level lower than the Reynolds stress closure model. In the  $k$ - $\varepsilon$  model, instead of seeking the direct closure of the Reynolds stress transport equations, an eddy viscosity assumption is made to relate the Reynolds stress  $\vec{\tau}$  in Equation (2) to the turbulence kinetic energy  $k$  and the strain rate of the mean flow as

$$\tau_{ij}/\rho = 2\nu_T S_{ij} - \frac{2}{3}k\delta_{ij} \quad (3)$$

where  $S_{ij} = \frac{1}{2}(\partial u_i/\partial x_j + \partial u_j/\partial x_i)$  is the mean strain rate,  $\nu_T$  the turbulence eddy viscosity, and  $\delta_{ij}$  the Kronecker delta.

By assuming the local balance between the turbulence production and dissipation and using a dimensional analysis, the relationship between the turbulence eddy viscosity  $\nu_T$ , turbulence energy  $k$  and turbulence dissipation rate  $\varepsilon$  is established as follows:

$$\nu_T = c_d \frac{k^2}{\varepsilon} \quad (4)$$

where  $c_d$  is the empirical constant.

The  $k$  and  $\varepsilon$  transport equations are derived based on the N-S equations and represented also in the following Lagrangian form for the SPH approach:

$$\frac{Dk}{Dt} = \nabla \cdot \left( \frac{\nu_T}{\sigma_k} \nabla k \right) + P_k - \varepsilon \quad (5)$$

$$\frac{D\varepsilon}{Dt} = \nabla \cdot \left( \frac{\nu_T}{\sigma_\varepsilon} \nabla \varepsilon \right) + c_{1\varepsilon} \frac{\varepsilon}{k} P_k - c_{2\varepsilon} \frac{\varepsilon^2}{k} \quad (6)$$

where  $\sigma_k$ ,  $\sigma_\varepsilon$ ,  $c_{1\varepsilon}$  and  $c_{2\varepsilon}$  are other empirical constants, and  $P_k$  is the turbulence production rate defined by the resolved mean flows.

Although the closure assumptions employed in the  $k$ - $\varepsilon$  equations are relatively crude, this model has been successfully used to predict many complex flows. The recommended values for the empirical coefficients have been given by Rodi [23] as  $c_d = 0.09$ ,  $\sigma_k = 1.0$ ,  $\sigma_\varepsilon = 1.3$ ,  $c_{1\varepsilon} = 1.44$  and  $c_{2\varepsilon} = 1.92$ . According to Lin and Liu [16], a sensitivity analysis on these parameters showed that a 10% change in  $\sigma_k$ ,  $\sigma_\varepsilon$  and  $c_{2\varepsilon}$  only caused less than 10% change in the total turbulence energy, while a 10% change in  $c_{1\varepsilon}$  could lead to more than 50% change in the turbulence energy. In spite of some uncertainties involved, the recommended values are still adopted for the current SPH computations and the results indicate that they work reasonably well.

Here it should also be mentioned that these standard values of the turbulence constant represent a compromise chosen to give the best performance for a range of flows. For any particular flow it is likely that the accuracy of the model calculations can be improved by adjusting the constants. For example,  $c_{2\varepsilon} = 1.77$  is more suitable than  $c_{2\varepsilon} = 1.92$  for the decaying turbulence and  $c_{1\varepsilon}$  and  $c_{2\varepsilon}$  should be adjusted in order to better estimate the rate of spreading for the round jet. Besides, the empirical coefficients were selected largely on the basis of turbulent shear flows, so alternative values may be required in applications to flows that are dominated by extensive or compressive rates of strain. For a complete and accurate model, a single specification of all the constants may be required.

### 3. TWO-STEP EQUATION SOLVER

During the incompressible SPH computations, the governing equations (1) and (2) are solved through a prediction–correction two-step process, as stipulated by Shao and Lo [14] and Shao and Gotoh [20]. The solution processes are also similar to those formulated in the SPH projection method of Cummins and Rudman [15]. The first prediction step is an explicit integration in time without enforcing the incompressibility. Only the turbulent stresses, laminar viscosity and gravitational term in Equation (2) are used and thus an intermediate particle velocity and position are obtained

$$\Delta \mathbf{u}_* = \left( \mathbf{g} + \nu_0 \nabla^2 \mathbf{u} + \frac{1}{\rho} \nabla \cdot \vec{\tau} \right) \Delta t \quad (7)$$

$$\mathbf{u}_* = \mathbf{u}_t + \Delta \mathbf{u}_* \quad (8)$$

$$\mathbf{r}_* = \mathbf{r}_t + \mathbf{u}_* \Delta t \quad (9)$$

where  $\Delta \mathbf{u}_*$  is the increment of particle velocity during the prediction step,  $\Delta t$  the time increment,  $\mathbf{u}_t$  and  $\mathbf{r}_t$  the particle velocity and position at time  $t$ , and  $\mathbf{u}_*$  and  $\mathbf{r}_*$  the intermediate particle velocity and position.

In the second correction step, the pressure term is used to update the intermediate particle velocity obtained from the prediction step:

$$\Delta \mathbf{u}_{**} = - \frac{1}{\rho_*} \nabla P_{t+1} \Delta t \quad (10)$$

$$\mathbf{u}_{t+1} = \mathbf{u}_* + \Delta \mathbf{u}_{**} \quad (11)$$

where  $\Delta \mathbf{u}_{**}$  is the increment of particle velocity during the correction step,  $\rho_*$  the intermediate particle density after the prediction step, and  $P_{t+1}$  and  $\mathbf{u}_{t+1}$  the particle pressure and velocity at time  $t + 1$ .

Finally, the positions of particle are centred in time

$$\mathbf{r}_{t+1} = \mathbf{r}_t + \frac{(\mathbf{u}_t + \mathbf{u}_{t+1})}{2} \Delta t \quad (12)$$

where  $\mathbf{r}_t$  and  $\mathbf{r}_{t+1}$  are the positions of particle in time  $t$  and  $t + 1$ . Besides, the turbulence properties are updated according to Equations (5) and (6) after the mean flow fields have been resolved.

The pressure for updating the intermediate particle velocity in the correction step is calculated from the pressure Poisson equation as follows:

$$\nabla \cdot \left( \frac{1}{\rho_*} \nabla P_{t+1} \right) = \frac{\rho_0 - \rho_*}{\rho_0 \Delta t^2} \quad (13)$$

where  $\rho_0$  is the initial constant density at each of the particles. This equation is formulated by combining the mass and momentum equations (1) and (2) and imposing the true incompressibility. The formulation is analogous to that employed in the MPS method of Koshizuka *et al.* [9], in that the source term of the equation is the variation of particle densities, while it is usually the divergence of intermediate velocity in finite difference methods. This semi-implicit algorithm to calculate the pressures distinguishes the truly incompressible version of the SPH presented in the current paper from the original weakly compressible SPH of Monaghan [12], in which the following equation of state was employed to obtain the pressure in an explicit way:

$$P = B \left[ \left( \frac{\rho_*}{\rho_0} \right)^\gamma - 1 \right] \quad (14)$$

where  $B$  is the parameter chosen to ensure the sound speed is a factor 10 larger than the typical fluid velocity in the model and  $\gamma \approx 7$  is another constant. Equation (14) could cause pressure fluctuations due to the introduction of empirical constants and the assumption of large sound speed. In comparison, the real incompressible formulation of Equation (13) is derived directly from the basic hydrodynamic equations and thus free of assumptions.

For the purpose of efficient computations, the time step  $\Delta t$  is dynamically adjusted in the simulations based on the constraint of Courant condition and viscous diffusion. Also a particle-link list should be generated to identify the neighbouring particles to expedite the searching process. These acceleration techniques effectively reduce the computational load from  $N^2$  to  $N$ , where  $N$  is the particle numbers.

#### 4. REVIEW OF SPH CONCEPTIONS AND FORMULATIONS

The advantages of SPH arise directly from its Lagrangian nature. Since there is no mesh distortion, it can effectively deal with large deformations and multi-surfaces in a pure Lagrangian frame. In the SPH concept, the motion of each particle is calculated through interactions with neighbouring particles by an analytical kernel function. All terms in the governing equations

are represented through such particle interaction models and thus a grid is not needed. The underlying assumption of SPH is that any field variable of a reference particle can be expressed with enough accuracy by integrals which are approximated by summation interpolants over neighbouring particles. Furthermore, the spatial derivatives such as the gradient and divergence can be similarly evaluated by summation interpolants. The SPH equations describe the motion of the interpolating points, which can be conceptually thought as particles. Each particle can carry a mass  $m$ , a velocity  $\mathbf{u}$ , and other properties depending on the problem. For the turbulence modelling, a particle also carries the turbulence eddy viscosity  $\nu_T$ , turbulence energy  $k$  and energy dissipation  $\varepsilon$ . For a detailed review of SPH theory see Reference [12].

Using the above concepts, any quantity of particle  $a$ , whether scalar or vector, can be approximated by the direct summation of the relevant quantities of its neighbouring particles  $b$

$$\varphi_a(\mathbf{r}_a) = \sum_b m_b \frac{\varphi_b(\mathbf{r}_b)}{\rho_b(\mathbf{r}_b)} W(|\mathbf{r}_a - \mathbf{r}_b|, h) \quad (15)$$

where  $a$  and  $b$  are the reference particle and its neighbours,  $\varphi_a$  and  $\varphi_b$  the scalar or vector quantity being interpolated and interpolating,  $\mathbf{r}_a$  and  $\mathbf{r}_b$  the position of particles,  $W$  the interpolation kernel, and  $h$  the smoothing distance. It determines the range with which a particle interacts with neighbouring particles. In subsequent computations  $h$  is set to be twice the initial particle spacing.

Thus, the fluid density  $\rho_a$  of particle  $a$  is evaluated by

$$\rho_a = \sum_b m_b W(|\mathbf{r}_a - \mathbf{r}_b|, h) \quad (16)$$

Kernels can assume many different forms and the use of different kernels is the SPH analogue of using different difference schemes in finite difference methods. By balancing the computational accuracy and efficiency, the kernel based on the spline function and normalized in 2-D is adopted [12].

The gradient term has different forms depending on the derivation used. The following symmetric form is widely used since it conserves linear and angular momentum exactly:

$$\left( \frac{1}{\rho} \nabla P \right)_a = \sum_b m_b \left( \frac{P_a}{\rho_a^2} + \frac{P_b}{\rho_b^2} \right) \nabla_a W_{ab} \quad (17)$$

where the summation is over all particles other than particle  $a$  and  $\nabla_a W_{ab}$  is the gradient of the kernel taken with respect to the positions of particle  $a$ . Similarly, the divergence of a vector  $\mathbf{u}$  at the position of particle  $a$  can be formulated symmetrically by

$$\nabla \cdot \mathbf{u}_a = \rho_a \sum_b m_b \left( \frac{\mathbf{u}_a}{\rho_a^2} + \frac{\mathbf{u}_b}{\rho_b^2} \right) \cdot \nabla_a W_{ab} \quad (18)$$

For the purpose of particle pressure stability, the Laplacian is formulated as a hybrid of a standard SPH first derivative with a finite difference approximation for the first derivative, following the original formulation of Cummins and Rudman [15] but representing it in symmetric form as

$$\nabla \cdot \left( \frac{1}{\rho} \nabla P \right)_a = \sum_b m_b \frac{8}{(\rho_a + \rho_b)^2} \frac{P_{ab} \mathbf{r}_{ab} \cdot \nabla_a W_{ab}}{|\mathbf{r}_{ab}|^2} \quad (19)$$

where abbreviations  $P_{ab} = P_a - P_b$  and  $\mathbf{r}_{ab} = \mathbf{r}_a - \mathbf{r}_b$  are introduced.

The turbulent stresses in Equation (2) are formulated by applying the SPH definition of divergence

$$\left(\frac{1}{\rho}\nabla\cdot\vec{\tau}\right)_a=\sum_b m_b\left(\frac{\vec{\tau}_a}{\rho_a^2}+\frac{\vec{\tau}_b}{\rho_b^2}\right)\cdot\nabla_a W_{ab} \quad (20)$$

With regard to the laminar stress in Equation (2), it simplifies to

$$(v_0\nabla^2\mathbf{u})_a=\sum_b m_b\frac{2(v_a+v_b)}{\rho_a+\rho_b}\frac{\mathbf{u}_{ab}\mathbf{r}_{ab}\cdot\nabla_a W_{ab}}{|\mathbf{r}_{ab}|^2} \quad (21)$$

where  $\mathbf{u}_{ab}=\mathbf{u}_a-\mathbf{u}_b$ .

## 5. TREATMENT OF BOUNDARY CONDITIONS AND FREE SURFACES

### 5.1. Identification of free surfaces

In the SPH model, free surfaces can always be easily identified and tracked by particles. Since there is no particle existing in the outer region of the free surface, the particle density on the free surface drops abruptly. This criterion to define the free surface is very simple and stable even under the fragmentation and coalescence of waters such as the plunging and splashing, according to Koshizuka *et al.* [9]. A particle is regarded as a surface particle if the absolute value of the difference between the particle density and reference density exceeds  $0.01\rho_0$ . At the free surface, the viscous effect is ignored for simplicity in the present case and this leads to a simplified normal dynamic free surface boundary condition. We just give a zero pressure to each of surface particles. The transition of surface and inner fluid particles is allowed in case of the broken surfaces.

### 5.2. Initial conditions

The initial conditions are implemented by setting all particle velocities  $\mathbf{u}=0$  in the computational domain at time  $t=0$ . Besides, the pressure distribution is assumed to be hydrostatic at the beginning of computation.

### 5.3. Fixed solid boundaries

Fixed solid boundaries such as the sea bottom and sloping sea wall are simulated by fixed wall particles, which balance the pressure of inner fluid particles and prevent them from penetrating the wall. Different from the treatment of wall particles using an explicit force function in the original SPH formulation of Monaghan [12], the pressure Poisson equation (13) is solved on wall particles in the truly incompressible SPH scheme. This is quite similar to the implementation widely found in a grid method. The velocities of wall particles are set to be zero to represent the no-slip boundary conditions. In order to impose the homogeneous Neumann boundary condition on wall particles, several lines of dummy particles are put on the other side of the wall and the pressure of these dummy particles is set to be equal to the pressure of neighbouring wall particles. Thus, the normal pressure gradient of wall particles is approximately zero and we only consider the interactions of neighbouring wall particles and inner fluid particles while solving the pressure equation.



#### 5.4. Offshore and onshore wave boundaries

The upstream open boundary is the incident wave boundary, which is modelled by a numerical wave maker also composed of wall particles. During the computation, the wave maker moves periodically and its frequency and amplitude are adequately adjusted until the desired incident wave profile is obtained. Following Hayashi *et al.* [10], the wave maker is designed to be able to produce an incident wave and meanwhile, absorb reflected waves from the downstream. The downstream open boundary is the so-called radiation boundary so that the wave is outgoing without strong reflections that may disturb the inner computational domain. It was found from the previous SPH trials for a simple test of wave propagating over constant depth that the above absorbing-generating boundary at the upstream inlet leads to  $\sim 5\%$  reflection of the total waves and the radiation boundary at the downstream outlet transmits  $\sim 95\%$  of the total waves. However, the downstream radiation boundary is not used in the present computations, since we consider the wave breaking and overtopping of a sloping sea wall.

#### 5.5. Turbulent boundaries and surfaces

Appropriate surface and boundary conditions are also needed for the turbulence properties. On the free surface, the zero-gradient boundary conditions are imposed for both  $k$  and  $\varepsilon$  to ensure the advective and diffusive fluxes of  $k$  and  $\varepsilon$  to be zero, i.e.  $\partial k / \partial n = 0$  and  $\partial \varepsilon / \partial n = 0$ , where  $n$  is the unit normal on the free surface. For the SPH particles, this requirement is achieved by setting the values of  $k$  and  $\varepsilon$  of the surface particles equal to those of the particles immediately underneath free surface in the normal direction. Thus, there is no turbulence exchange between the air and water.

In theory, the turbulence vanishes on the solid walls so that both  $k$  and  $\varepsilon$  become zero on the wall. However, in practice, the numerical resolution cannot be so fine as to resolve the viscous sub-layer. Thus, the boundary conditions for  $k$  and  $\varepsilon$  are generally specified in the turbulent boundary layer instead of right on the wall. Here we follow the approach of Lin and Liu [16] to use the log-law distribution of mean tangential velocities in the turbulent boundary layer, so that the values of  $k$  and  $\varepsilon$  can be expressed as the functions of distance from the solid boundary and the mean tangential velocities outside of the viscous sub-layer. Generally speaking, the commonly used log-law distribution is employed for the solid boundary.

For the  $k$ - $\varepsilon$  model, it is also necessary to seed a small amount of  $k$  and  $\varepsilon$  in the initial and inflow boundary conditions. Lin and Liu [16] and Bradford [17] used different approaches to seed the initial turbulence properties and unanimously found that the final computational results were insensitive to the initial seeding. The same conclusion was also drawn by Shao [22] in an incompressible SPH simulation of spilling and plunging breakers. In this paper, we reasonably assume that the initial condition should be described in such a way to satisfy  $v_T \approx v_0$ , while at the inflow boundary  $v_T \approx 10v_0$  should be applied. It means that the initial turbulence level is quite low in the inner fluid region and slightly higher near the inflow boundary. This leads to the initial seeding values of  $k = 2 \times 10^{-5} \text{ m}^2/\text{s}^2$  and  $\varepsilon = 4 \times 10^{-5} \text{ m}^2/\text{s}^3$  for the inner fluids and  $k = 2 \times 10^{-3} \text{ m}^2/\text{s}^2$  and  $\varepsilon = 4 \times 10^{-2} \text{ m}^2/\text{s}^3$  for the inflow boundary. The similar turbulent parameters were employed in the SPH computations of Shao [22].

A sensitivity analysis based on the SPH runs shows that the initial seeding has no obvious influence on the CPU time and final computational results. However, it does cause some differences in the beginning of computations and in the prediction of wave breakings. For

example, the smaller seeding of  $k$  can slightly delay the initial breaking processes, and vice versa. The same conclusions were also drawn by Lin and Liu [16] using an RANS modelling approach.

## 6. MODEL APPLICATION—WAVE BREAKING AND OVERTOPPING OF A SLOPING SEA WALL

Wave overtopping of a sea wall is a practical issue in the coastal engineering which can cause the failure of defence structures. The overtopping flows can become highly turbulent due to the presence of wave breaking and the interactions between the shoreward propagating bores and bores partially reflected from the structure. Here the incompressible SPH approach with  $k-\varepsilon$  modelling is employed to investigate regular waves overtopping of a smooth impermeable sea wall, which is also a well-known engineering design problem. The computations are compared with the experimental and numerical results of Li *et al.* [8]. They used a time-implicit cell-staggered approximately factored VOF finite volume approach for solving the unsteady incompressible N-S equations based on the non-uniform Cartesian cut-cell grids. Meanwhile, the effects of turbulence were addressed by using both static and dynamic sub-grid scale (SGS) LES turbulence models in their formulations.

### 6.1. Numerical wave flume and computation parameters

The SPH computations were performed in a numerical wave tank as illustrated by Li *et al.* [8]. The computational domain covering a sea wall is 6.3 m long and 1.0 m high. The seaward slope of the sea wall is 1:6 and it is 1:3 for the landward slope. The crest height of sea wall is 0.8 m and the width is 0.3 m. The distance between the upper offshore boundary and the toe of the sea wall is 1.0 m. We define  $x=0.0$  and 6.3 m as the inlet and outlet, respectively, and  $y=0.0$  as the original still water line. The initial constant water depth is  $d=0.7$  m. A regular wave with a height  $H=0.16$  m and period  $T=2.0$  s is used. According to the wave dispersion relationship, the corresponding wavelength is calculated to be  $L=4.62$  m. The sketch view of the numerical flume and configurations of the sea wall are shown in Figure 1. The time-dependent water surface elevations denoted by WG0–WG5 were measured at several locations in the experiment and compared with the present SPH computations and finite volume computations of Li *et al.* [8]. WG5 is located at  $x=5.9$  m on the sea wall crest, which is the area of particular interest in the study of wave overtopping events. Locations WG4, WG3, WG2 and WG0 correspond to  $x=5.20$ , 3.81, 2.02 and 0.0 m, respectively.

During the initial particle set up, a uniform particle spacing  $\Delta X=0.02$  m is used, which is fine enough to capture the general flow features during the wave overtopping and breaking processes, such as the free surface deformations and velocity structures. This resolution is the same order as the finest grid of  $251 \times 40$  (corresponding to a grid spacing of  $\Delta X=0.025$  m) used by Li *et al.* [8]. By using this particle configuration, a total number of  $N=6000$  particles are involved in the SPH simulations, including 400 wall particles for constituting the offshore wave maker, the sea bottom and the sloping sea wall. The overtopped fluid particles are continuously removed out of the computational domain for the purpose of maintaining the numerical stability. This treatment of the outflow boundary by particles is obviously consistent

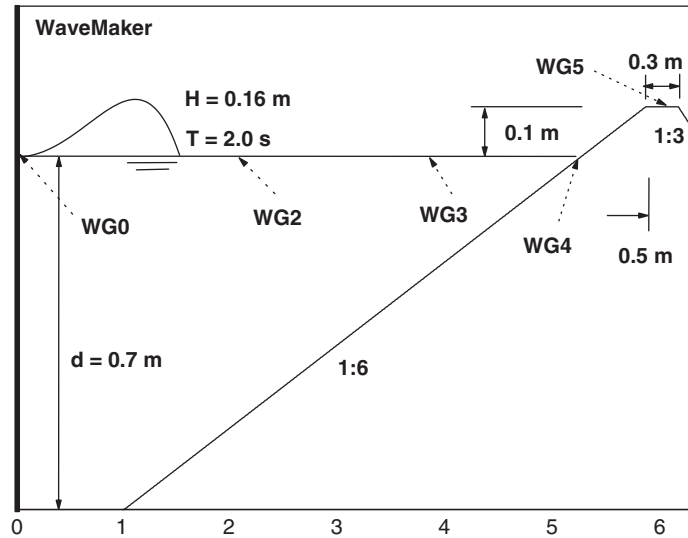


Figure 1. Sketch view of numerical flume and sloping sea wall for wave overtopping [8].

with the practical scenarios. The total loss of fluid mass is about 3% for 10 wave periods and has no great effect on the general simulations, since the overtopping is not severe in the present case.

## 6.2. Wave breaking and overtopping scenarios

For a general picture of the wave breaking and overtopping processes, the instantaneous particle snapshots and velocity fields during the overtopping within one wave period  $T$  are shown in Figures 2 and 3(a)–(c), respectively, based on the incompressible SPH computational results. The numerical data were extracted at  $t = 11.8$ ,  $12.5$  and  $13.2$  s. The simulated flow patterns are very similar to the finite volume computations of Li *et al.* [8] and both numerical models predicted complicated flow structures due to the wave breaking and overtopping.

Wave overtopping is a highly complicated process, including the wave attack, run-up, run-down, breaking and overtopping, accompanied by the large deformations of the free surface. As shown in Figures 2(a) and 3(a), some particles of the preceding wave still continue to overtop over the sea wall crest, while the majority of flows have already begun to retreat from the slope due to the gravitational acceleration. The retreating flows meet the next approaching wave and this leads to a strong backwash near  $x = 4.2$  m. The wave breaks violently, evidenced by the large deformation of free surface and the formation of a roller and large hydraulic jump. The wave continues to break and run up the slope at  $t = 12.5$  s, with the energy dissipated by the turbulence and advected by the vortices, which is manifested by the decreasing velocities in the wave front. Finally, the waves overtop of the sea wall at  $t = 13.2$  s

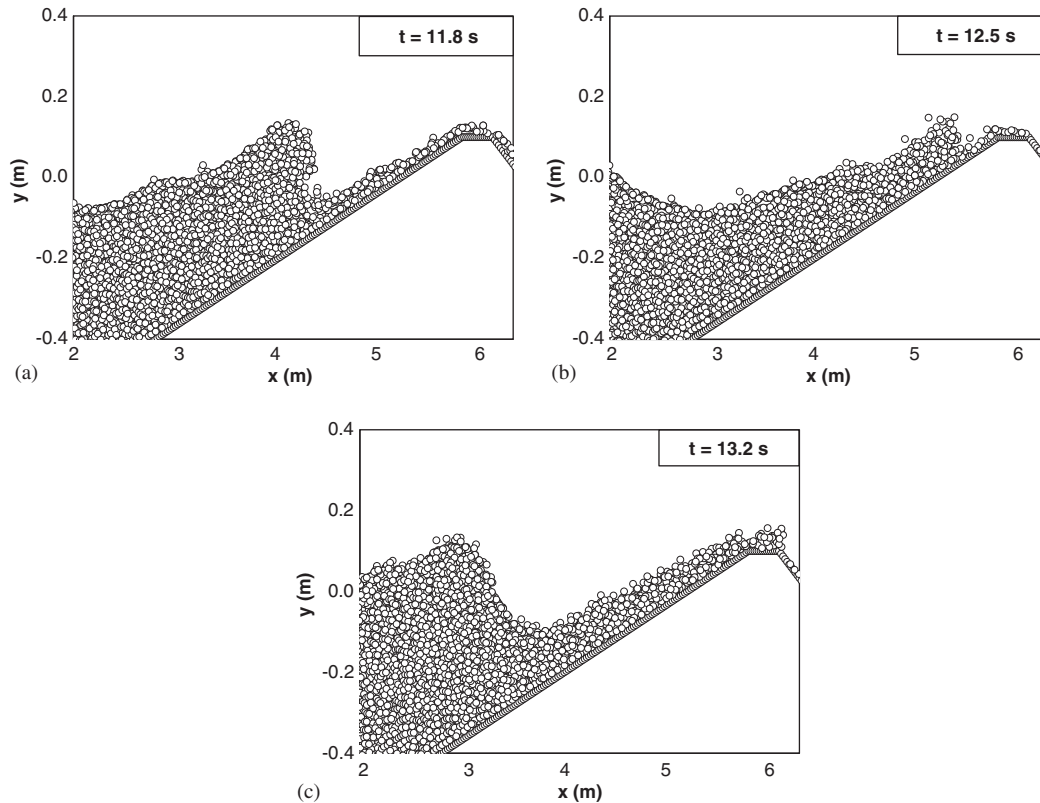


Figure 2. Particle snapshots during wave breaking and overtopping.

and an obvious overtopping jet shoots over the sea wall crest, as shown in Figures 2(c) and 3(c). However, it can be seen that the present wave overtopping is not so strong, since the sea wall crest is nearly at the same elevation as the incident wave crest and the incoming waves have already dissipated most of energy through the wave breaking prior to the overtopping.

One of the great advantages of the numerical models is their ability to disclose the evolutions of turbulence fields in the spatial and temporal domains. Based on the  $k-\varepsilon$  turbulence modelling, the turbulence kinetic energy distributions during the wave breaking and overtopping are shown in Figure 4(a)–(c) in one wave period, from which the detailed processes of turbulence production, advection and dissipation are well understood. In Figure 4, the turbulence energy  $(2k)^{1/2}$  has been normalized by the wave celerity  $c = \sqrt{gd}$  and only high-turbulence areas are plotted for illustration. It is shown from Figure 4(a) that  $(2k)^{1/2}/c$  increases to the maximum due to the influence of wave breaking. The computations clearly show the tendency that the wave crest curls and plunges forward into the water surface, which is an indication of a typical plunging breaker. This is also supported by the calculated surf similarity parameter  $\xi = S_0/\sqrt{H_0/L_0} = 0.958$ , based on the deep-water wave and slope parameters ( $S_0 = 1/6$ ,  $H_0 = 0.189$  m and  $L_0 = 6.245$  m). After the initial wave breaking, Figure 4(b) shows that the wave energy has been greatly dissipated and the turbulence is advected with the wave

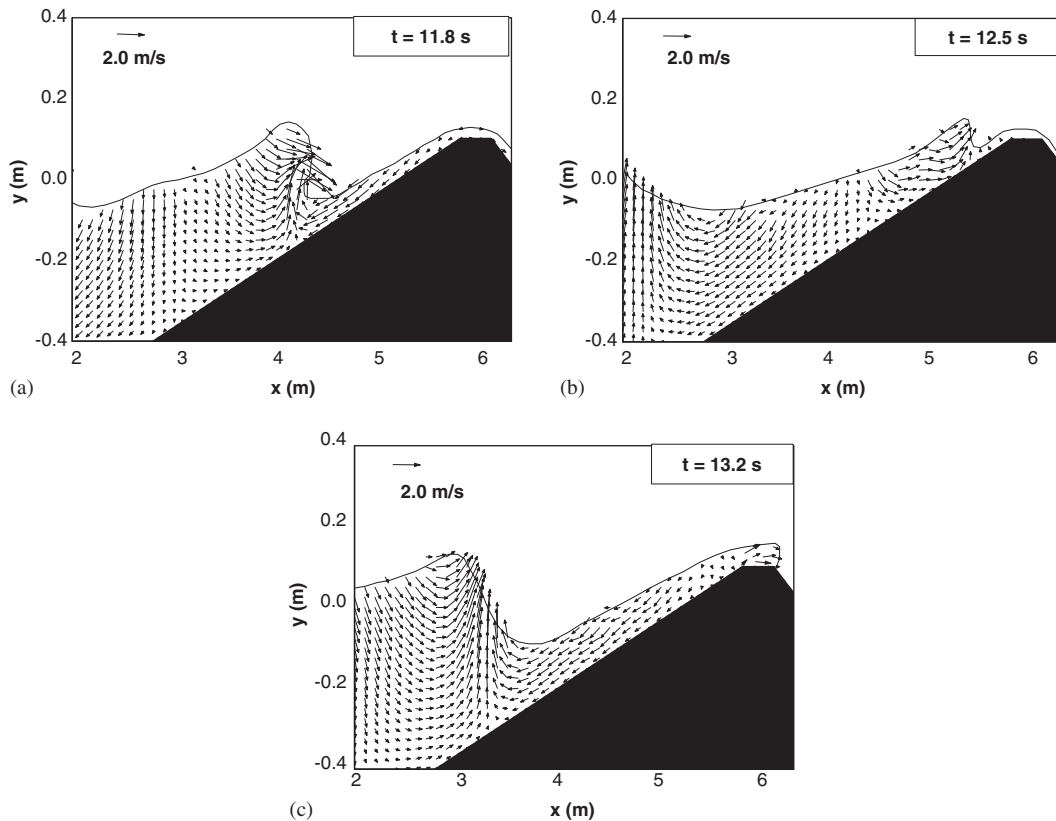


Figure 3. Velocity fields during wave breaking and overtopping.

front running up the slope. The peak turbulence energy  $(2k)^{1/2}/c$  is only 45% of the previous value at breaking. Figure 4(c) shows that  $(2k)^{1/2}/c$  increases again due to the wave overtopping over the sea wall crest and the maximum  $(2k)^{1/2}/c$  appears at the overtopping jet. Meanwhile, slightly higher turbulence quantities start to appear in the next wave front. This is an indication of the production of turbulence due to the incoming wave shoaling and pre-breaking deformation over the slope.

The turbulence eddy viscosity is another important parameter which measures the mixing rate for both momentums and substances. We also studied the evolutions of the computed eddy viscosities and found that the eddy viscosity has a different distribution pattern from that of the turbulence kinetic energy. As the water depth decreases, the eddy viscosity decreases much faster in the onshore direction than the turbulence quantity. This is mainly caused by the fact that the eddy viscosity is proportional to the turbulence length scale and turbulence energy  $(2k)^{1/2}$ , both of which simultaneously decrease as the water depth decreases. Much more detailed explanations can be found in Reference [16].

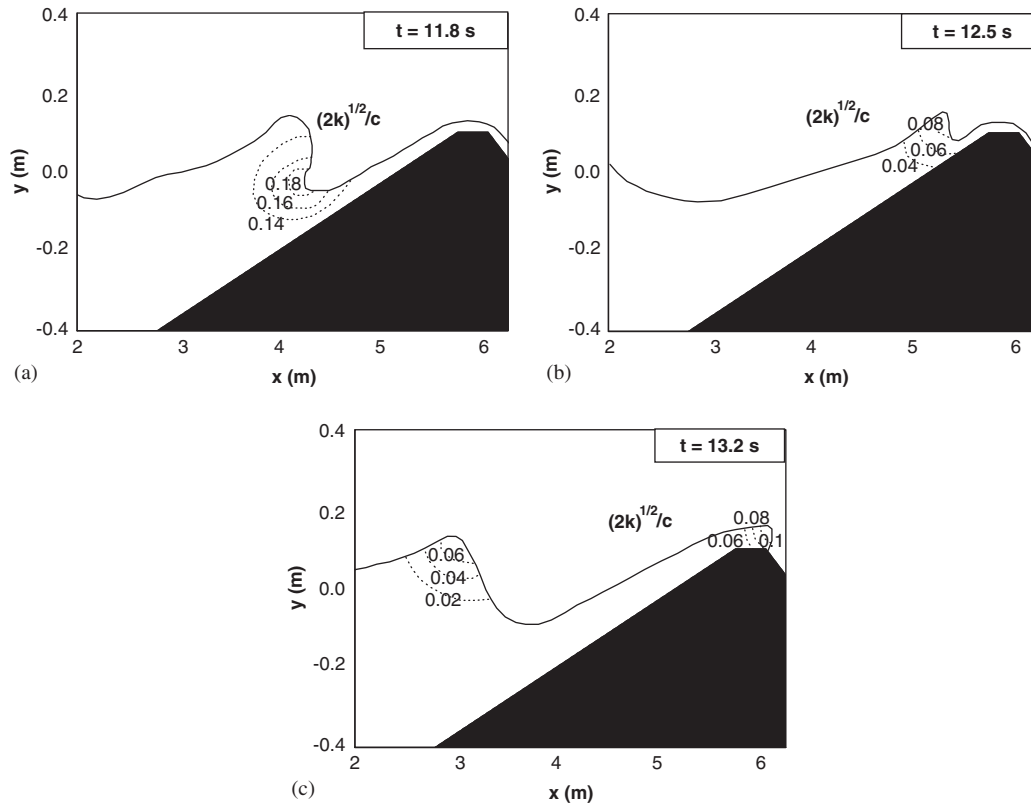


Figure 4. Turbulence kinetic energy distributions during wave breaking and overtopping.

### 6.3. Comparisons of water surface

For a quantitative evaluation of the incompressible SPH computations with  $k-\epsilon$  modelling, the computed water surface elevations at four gauging stations are shown in Figure 5(a)–(d), respectively. They correspond to WG2 ( $x = 2.02$  m), WG3 ( $x = 3.81$  m), WG4 ( $x = 5.2$  m) and WG5 ( $x = 5.9$  m), in which WG4 is located in the surf zone and WG5 is located on the sea wall crest. Meanwhile, the experimental and numerical data of Li *et al.* [8] are shown for a comparison. The experimental data are only available for WG2 and WG3 and all the data shown in the figure correspond to the time between  $t = 20.0$  and  $22.0$  s. The numerical data of Li *et al.* [8] were calculated from the finest grid of  $251 \times 40$  and using a dynamic Smagorinsky model, since they gave the best numerical performance. At WG5 the surface elevation is calculated with respect to the sea wall crest. It should be mentioned here that the experimental and numerical data of Li *et al.* [8] were extracted from their original paper and thus the plotting resolutions in the figure must be lower than the original work.

It is shown from Figure 5 that the general agreement between the experimental data and numerical computations by SPH and Li *et al.* [8] is quite satisfactory. All results indicate a feature of typical non-linearity, i.e. higher and narrower wave crest accompanied by a lower and flatter wave trough. In the areas of WG3 (close to breaking point), WG4 (surf zone) and

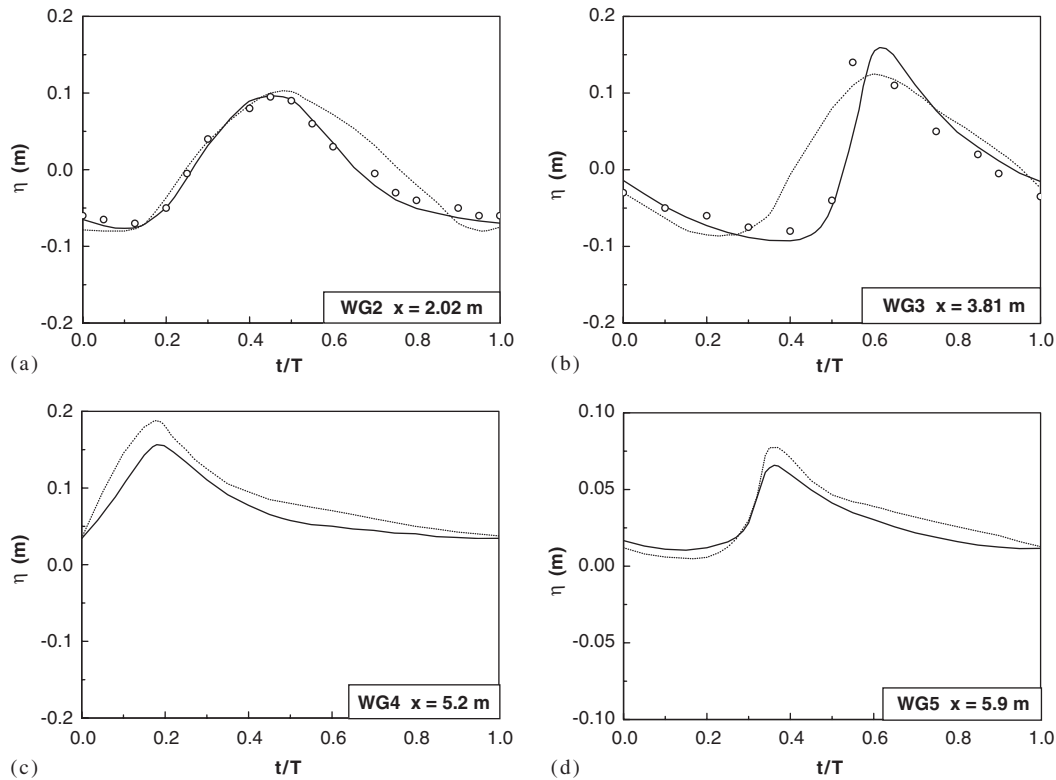


Figure 5. Comparisons of computed water surface elevations by SPH (solid lines) with experimental (circles) and numerical (dotted lines) data of Li *et al.* [8].

WG5 (sea wall crest), the wave profiles increase rapidly at first and then diminish slowly during one wave period, consistent with the non-linear wave theory. As shown in Figure 5(a) and (b), the SPH computations produce better results than those of Li *et al.* [8], according to the experimental data. The good agreement is mainly attributed to the fact that the free surfaces are accurately tracked by particles without numerical diffusion in the SPH approach.

In Figure 5(c) at WG4 and Figure 5(d) at WG5, the SPH computations predict smaller water surface levels than those predicted by Li *et al.* [8], although the tendency of two numerical wave profiles are consistent with each other both in the phase and in the shape. The differences are thought to partly arise from the different turbulence models used in the two numerical simulations. Li *et al.* [8] employed a dynamic Smagorinsky model for the finite volume computations, in which the Smagorinsky constant is an adjustable parameter depending on the flow properties. On the other hand, the incompressible SPH method employs a two-equation  $k-\varepsilon$  model for the turbulence. In spite of the fact that  $k-\varepsilon$  model has been widely and successfully applied in most fields in the river engineering, the source of prediction discrepancies could be traced to the use of constant empirical coefficients in the model. These coefficients were derived from the quasi-steady flows and thus may behave poorly in strongly transient turbulence flows such as the breaking wave. The  $k-\varepsilon$  model tends to overpredict the turbulence levels for breaking waves and underpredict the corresponding wave surface

profiles due to excessive turbulence dissipation. The same problem was also reported by Lin and Liu [16] for a breaking wave simulation using an RANS approach. The  $k-\varepsilon$  model was established on the basis of time-averaging process while the flow unsteadiness is very strong during the wave breaking. Thus, the applications of  $k-\varepsilon$  model in surf zone hydrodynamics might need more justifications and vigorous tests.

## 7. SENSITIVITY ANALYSES OF NUMERICAL MODEL

In this section, we use a series of numerical runs and tests based on the previous wave overtopping case to investigate the influence of turbulence modelling and particle numbers (spatial resolution) on the simulation results. The similar issues were also addressed by Li *et al.* [8] using a finite volume approach and their findings are used here for a comparison.

### 7.1. Conservation of incompressibility

Conservation of mass or incompressibility provides a convincing self-check on the accuracy for incompressible numerical models. For the incompressible SPH model proposed in the paper, a quantitative measurement of the conservation of incompressibility is provided by evaluating the differences of time-dependent particle densities  $\rho(t)$  with the initial values  $\rho_0$ . It is calculated as the averaged density variation of all particles, normalized with respect to the initial density [14, 20]:

$$E(t) = \frac{1}{N} \sum_{i=1}^N \text{abs}[\rho_i(t) - \rho_0] / \rho_0 \quad (22)$$

In an ideal incompressible SPH computation, particles should be moved to positions to satisfy  $E(t)$  to be zero at all times. However, it is not realistic in practice and the local particle density errors cannot be avoided. The accumulation of density errors is to be expected. For any incompressible numerical scheme, the resulting divergence-free velocity or incompressibility is achieved only within a spatial truncation error either by the computational precision or by the numerical scheme itself. Errors in particle positions will lead to density errors. Similar problems were also reported in an SPH projection method of Cummins and Rudman [15] in the velocity fields. In a stable numerical computation, the particle density errors  $E(t)$  would also be expected to be stable.

For a quantitative analysis, the normalized time-dependent particle density errors  $E(t)$  are shown in Figure 6 based on the SPH computations. It is shown that the general accuracy of the incompressible SPH model is quite satisfactory in that the density errors are controlled within the order of  $10^{-2}$ . The density errors  $E(t)$  increase rapidly at the beginning of the computation and reach the maximum around  $t \approx 2.0$  s, which is the time scale required for the initial wave to fully develop in one wave period. Then  $E(t)$  continue to stabilize at around 2.0% without further increase even if the computations have been executed to  $10T$ . The calculated peak density error by the present incompressible SPH model is quite close to the value of 2.4% reported by Cummins and Rudman [15] using an SPH projection method for a vortex spin-down. Furthermore, it is found that the density errors  $E(t)$  are reduced by approximately 50% as the particle spacing is halved to  $\Delta X = 0.01$  m in a refined SPH computation, the result of



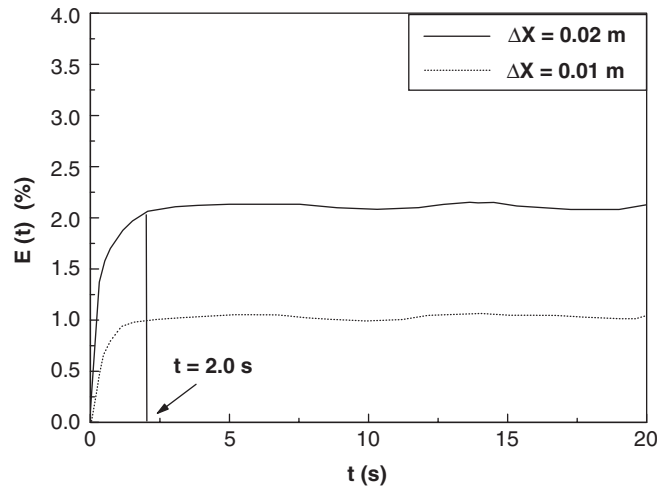


Figure 6. Time-dependent particle density errors of SPH computations using different particle spacing  $\Delta X$ .

which is shown in the same figure. This means that the improvement of spatial resolutions can effectively reduce the accumulations of errors in the density field.

### 7.2. Repeatability of wave overtopping

The repeatability of computations provides another useful check for the numerical models dealing with the periodical flow simulations. Since the waves are produced following the sinusoidal motions of a wave paddle in the computations, the wave overtopping should also have a repeatable occurrence. According to the SPH computations, the overtopping volume arising from each wave is given in Figure 7. It is shown that the difference between each flow due to the phase difference is very small and the periodical motion of the overtopping flows is well reproduced, suggesting that the numerical computations are quite stable even after long simulations. However, the exact repeatability cannot be maintained in practice, since the turbulence has a random nature and affects the repeatable flows. According to the statistical analyses of Figure 7, the mean overtopping volume in one wave is  $0.01 \text{ m}^3$  and the standard deviation is  $0.0005 \text{ m}^3$ . Thus, the mean overtopping rate is calculated to be  $0.005 \text{ m}^3/\text{s}$  ( $T = 2.0 \text{ s}$ ), which belongs to the moderate wave overtopping event by following the classifications in the relevant coastal manuals. It is suggested that this kind of wave overtopping could lead to both functional and structural damages if proper engineering measures are not taken.

### 7.3. Influence of turbulence modelling

In order to investigate the influence of turbulence model on the computation results, the incompressible SPH model was re-run by deactivating the  $k-\varepsilon$  turbulence model while keeping the remaining computational parameters unchanged. The computed particle snapshots and velocity fields within one wave period corresponding to Figures 2 and 3(a)–(c) (with the  $k-\varepsilon$  model activated) are shown in Figures 8 and 9(a)–(c), respectively. Compared with Figures 2

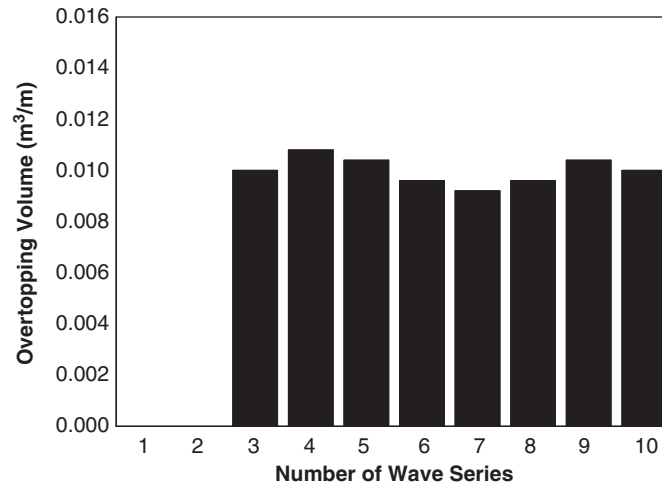


Figure 7. Computed overtopping volume for each wave.

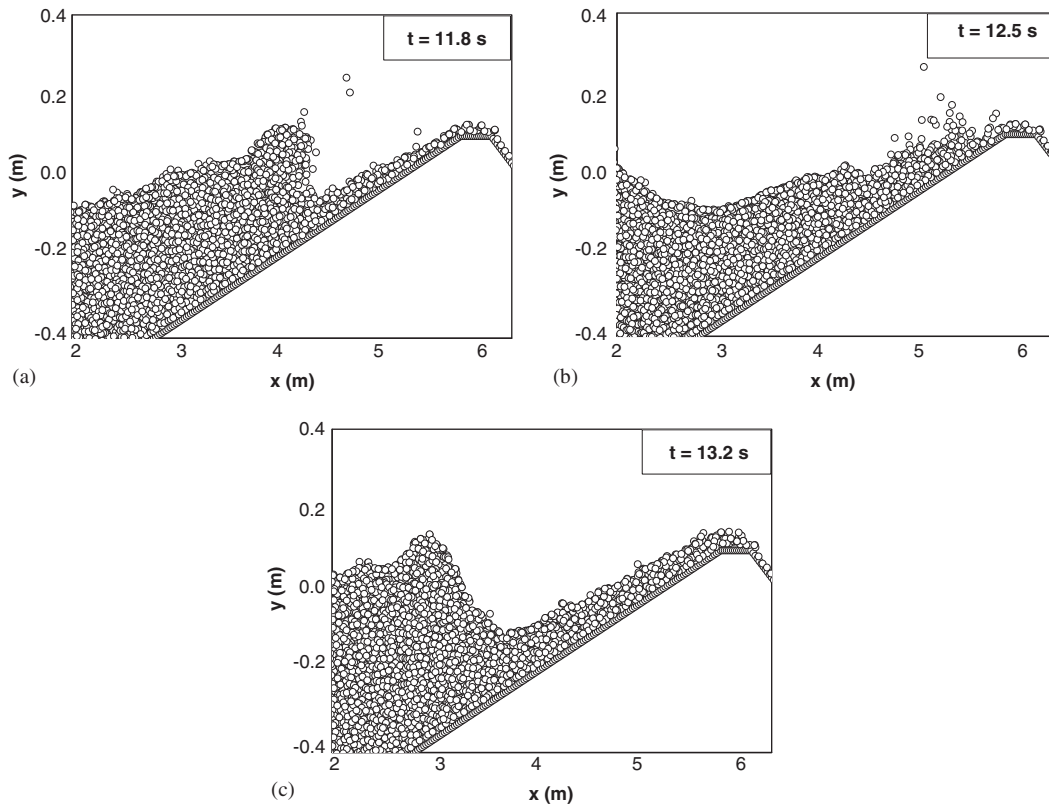


Figure 8. Particle snapshots during wave breaking and overtopping without turbulence modelling.

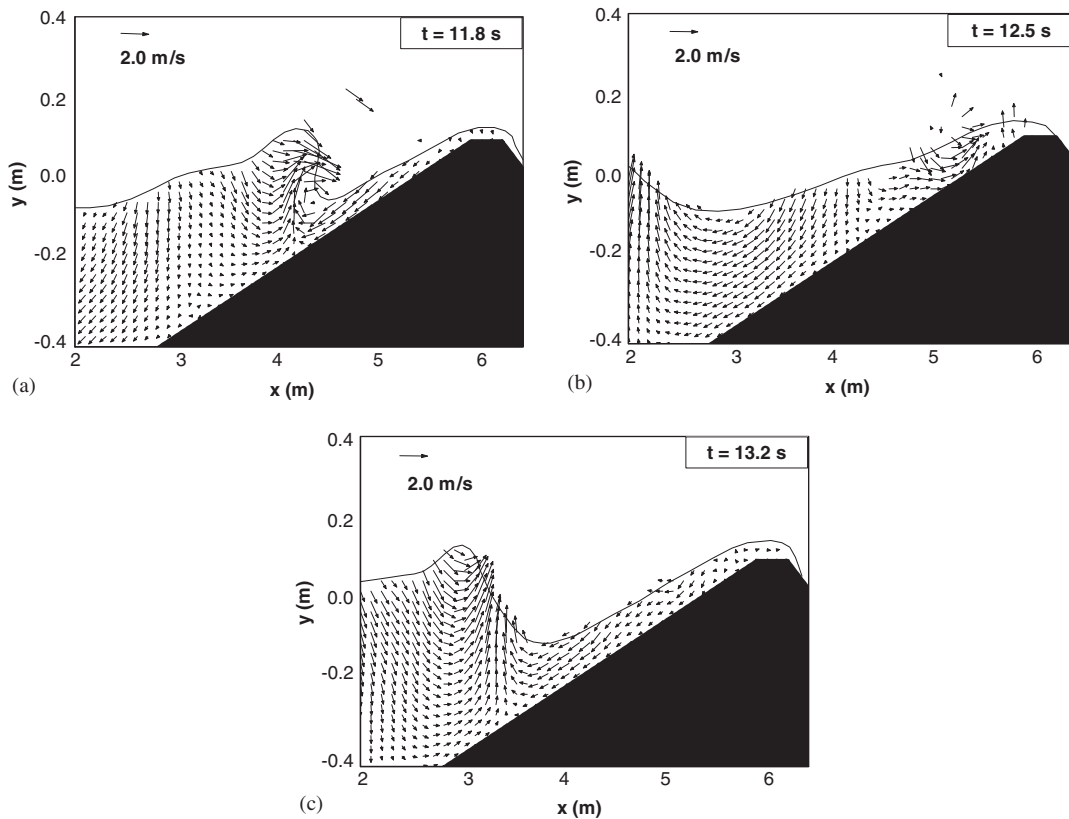


Figure 9. Velocity fields during wave breaking and overtopping without turbulence modelling.

and 3, it is shown that significant differences exist during the wave breaking and running up the slope at time  $t = 11.8$  and  $12.5$  s. The computations without the turbulence model predict spurious velocities near the wave front due to the lack of adequate turbulence dissipation, since the flows become highly turbulent when the waves continue to break in the surf zone. At time  $t = 13.2$  s, the overtopping jet over the sea wall crest calculated without the turbulence model seems to be much weaker. Besides, several individual particles overshoot out of the free surfaces as seen in Figure 8(a) and (b). This is also attributed to the absence of the turbulence model, which can guarantee the orderly particle motions and thus eliminate the excessive particle fluctuations, similar to the XSPH algorithm employed in the original weakly compressible SPH of Monaghan [12].

To quantitatively evaluate the effect of turbulence modelling, the computed water surface profiles without the  $k-\varepsilon$  turbulence model are compared with those obtained with the  $k-\varepsilon$  model and the experimental data of Li *et al.* [8] in Figure 10(a) and (b), at the gauging stations of WG2 and WG3, respectively, representing the region away from and close to the breaking zone. It is shown that the two numerical wave profiles in each figure deviate obviously from each other and the difference is more predominant in Figure 10(b) than in Figure 10(a). The

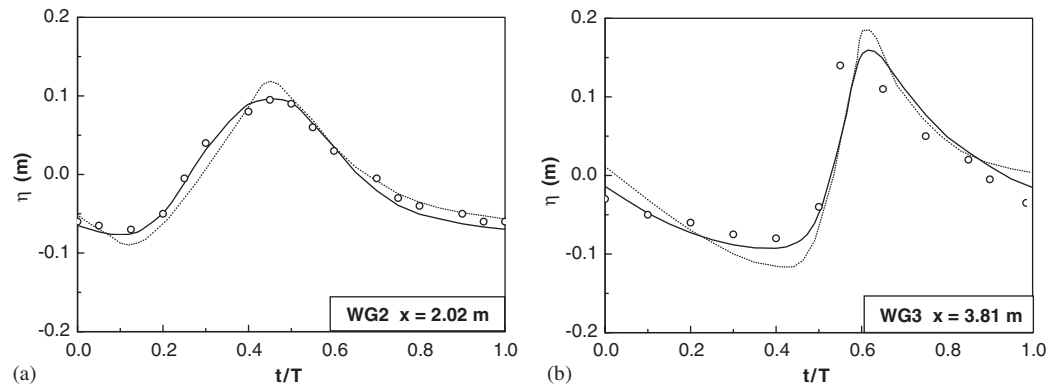


Figure 10. Comparisons of computed water surface elevations with (solid lines) and without (dotted lines) turbulence modelling with experimental data (circles) of Li *et al.* [8].

surface profiles computed without the turbulence modelling produce relatively higher wave heights due to the lack of turbulent dissipation. The maximum difference in the wave heights is 0.035 m in Figure 10(a) at WG2, while it is 0.05 m in Figure 10(b) at WG3, which is the region close to the breaking point.

The above findings indicate that the inclusion of an appropriate turbulence model has a profound influence on the simulations of wave breaking and overtopping, since the turbulence is quite strong and thus has a great effect on the mean flow fields. The potential flow model cannot adequately capture the energy dissipation in the practical situations and leads to the inaccurate flow predictions. A similar conclusion has already been drawn by Li *et al.* [8]. However, the non-turbulence SPH run did not exhibit any unrealistic large-scale vortex structures as reported by Li *et al.* [8], nor did another SPH run in which the laminar viscosity value was also set to zero.

#### 7.4. Influence of particle numbers/particle spacing

In order to study the influence of spatial resolutions (represented by the particle spacing  $\Delta X$ ) on the simulation results, the incompressible SPH model was also re-run using a finer particle spacing  $\Delta X = 0.01$  m and the results are compared with the original runs in which a particle spacing  $\Delta X = 0.02$  m was used. The finer spatial resolution is twice higher than the finest grid of  $251 \times 40$  (equivalent of a grid spacing of 0.025 m) used by Li *et al.* [8]. In this case, we have to move the offshore numerical wave paddle closer to the toe of the sea wall slope, thereby maintains the particle numbers around  $N = 18\,000$ .

The computed particle snapshots and velocity fields by using  $\Delta X = 0.01$  m are shown in Figures 11 and 12(a)–(c), respectively. In addition, the computed water surface elevations at WG2 ( $x = 2.02$  m) and WG3 ( $x = 3.81$  m) are compared with the original SPH runs ( $\Delta X = 0.02$  m) and the experimental data of Li *et al.* [8] in Figure 13(a) and (b). It is shown from Figure 13 that both SPH runs can equally capture the general wave profiles in a satisfactory way but the finer computations agree better with the experiment. Further, examining the particle snapshots and velocity fields of two SPH runs by comparing Figures 11 and 12 with Figures 2 and 3, suggests that more detailed flow features (such as the wave

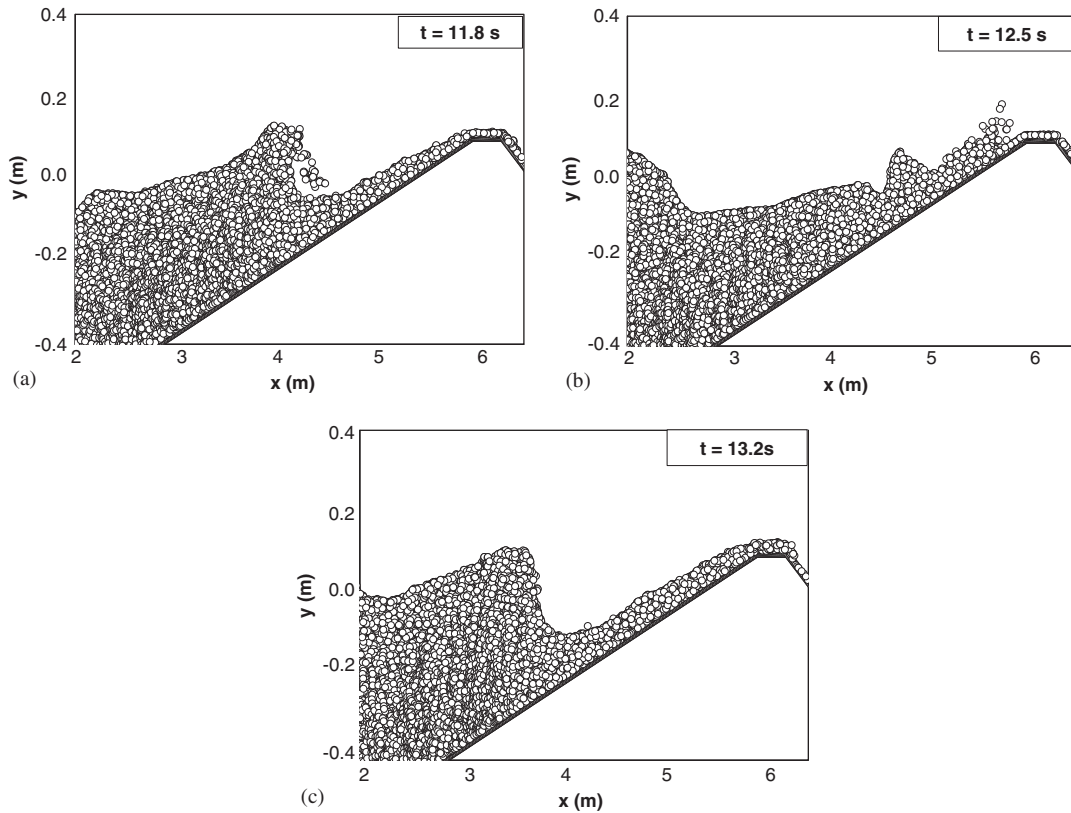


Figure 11. Particle snapshots during wave breaking and overtopping using refined particle spacing  $\Delta X = 0.01$  m.

breaking characteristics and velocity structures) are resolved by the finer particle size. For example, the finer SPH runs reproduce a strong breaking of the plunging wave. The comparisons indicate that the influence of particle size is relatively small for the water surfaces but large for the refined structures of the velocity field. This is due to the fact that some detailed small-scale flows are lost by using a coarser resolution.

## 8. CONCLUSIONS

The paper presents a truly incompressible version of the SPH method to investigate the water waves overtopping of a sea wall. The computations are in good agreement with the experimental data and numerical results from the literature. It is shown that the SPH method provides an accurate way of tracking large deformations of the free surface. The two-equation  $k-\varepsilon$  modelling reasonably discloses the turbulence evolution features during the wave breaking and overtopping, in spite of the fact that constant coefficients are used in the model. The SPH computations lead to better agreement of the wave surface profiles and reproduce the plunging

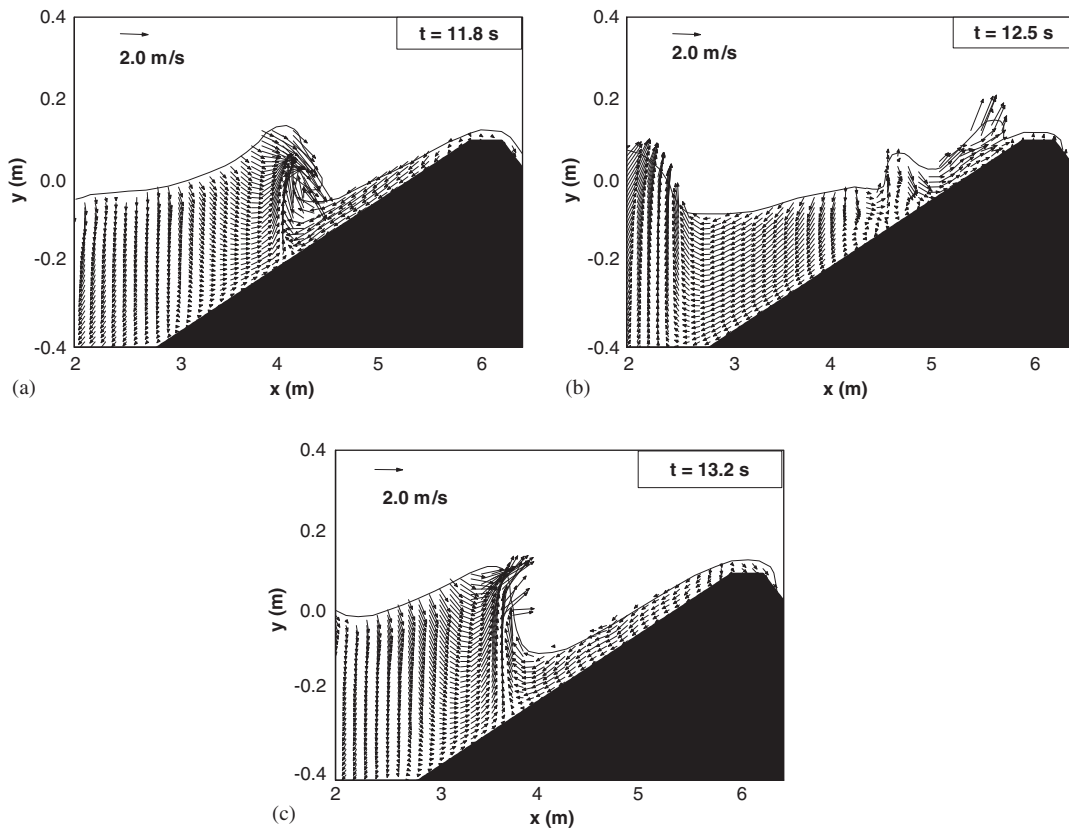


Figure 12. Velocity fields during wave breaking and overtopping using refined particle spacing  $\Delta X = 0.01$  m.

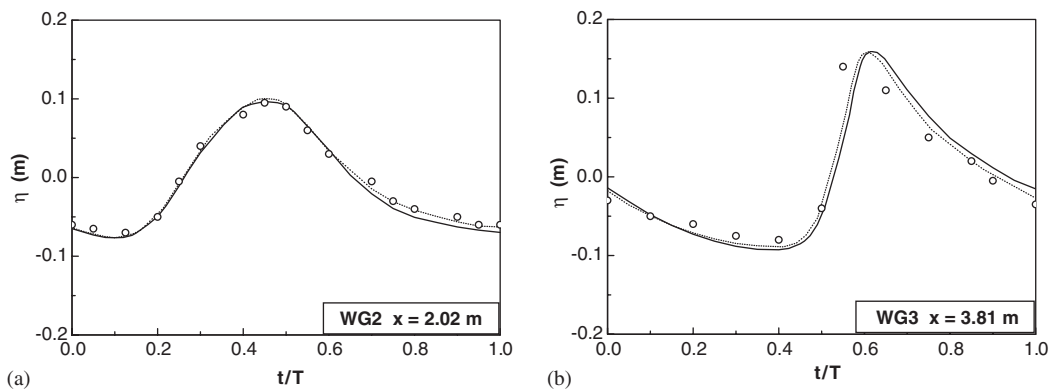


Figure 13. Comparisons of computed water surface elevations using particle spacing  $\Delta X = 0.02$  m (solid lines) and  $0.01$  m (dotted lines) with experimental data (circles) of Li *et al.* [8].

wave collapsing, running up and overtopping. The sensitivity analyses of the numerical model show that both turbulence modelling and spatial resolution play an important role in the computations and a finer particle resolution can disclose much more detailed flow structures.

Future work is needed to apply the SPH model to the random wave simulations, which are of greater practical interest.

## NOMENCLATURE

$B$	parameter for equation of state
$c$	wave celerity
$c_{1\varepsilon}$	turbulence constant
$c_{2\varepsilon}$	turbulence constant
$c_d$	turbulence constant
$d$	constant water depth
$E(t)$	time-dependent density error
$\mathbf{g}$	gravitational acceleration
$h$	kernel smoothing distance
$H$	wave height
$H_0$	deep-water wave height
$k$	turbulence kinetic energy
$L$	wave length
$L_0$	deep-water wave length
$m$	particle mass
$\mathbf{n}$	unit normal on free surface
$N$	particle numbers
$P$	pressure
$P_k$	turbulence production rate
$\mathbf{r}$	position vector
$S_0$	slope of beach
$S_{ij}$	element of strain
$T$	wave period
$\mathbf{u}$	velocity vector
$W$	interpolation kernel ( $\nabla_a W_{ab}$ = gradient of kernel)

### *Greek letters*

$\gamma$	constant for equation of state
$\delta_{ij}$	Kronecker's delta
$\Delta t$	time increment
$\Delta \mathbf{u}$	change in velocity
$\Delta X$	grid or particle spacing
$\varepsilon$	turbulence dissipation rate
$\nu_0$	kinetic viscosity of laminar flow
$\nu_T$	turbulence eddy viscosity
$\xi$	surf similarity parameter

$\rho$	density
$\rho_0$	initial density
$\sigma_k$	turbulence constant
$\sigma_\varepsilon$	turbulence constant
$\Rightarrow \tau$	turbulent Reynolds stress
$\tau_{ij}$	element of turbulent stress
$\varphi$	any quantity for interpolation

### *Subscripts and symbols*

$a$	reference particle
$b$	neighbouring particle
$ab$	values between particle $a$ and $b$
$t$	time
$x$	horizontal coordinate
$y$	vertical coordinate
$*$	intermediate value
$**$	corrective value

### ACKNOWLEDGEMENTS

The numerical SPH code in the paper was developed and improved from the Moving Particle Semi-implicit (MPS) program provided by Professor Seiichi Koshizuka, The University of Tokyo. The author is equally very grateful to Professor Edmond Yat-man Lo at Nanyang Technological University and Professor Hitoshi Gotoh at Kyoto University, for their constructive ideas and guidance on the SPH and turbulence modelling. Besides, the invaluable comments and discussions from Professor Dominic Reeve, Dr Phil James (Principal Lecturer), Dr David Graham (Principal Lecturer) and Professor Andrew Chadwick at the University of Plymouth significantly improved the quality of paper. The author also kindly acknowledges the support of the Japan Society for the Promotion of Science (JSPS) and the University of Plymouth provided through a postdoctoral research fellowship.

### REFERENCES

1. Liu PLF, Lin PZ, Chang KA, Sakakiyama T. Numerical modelling of wave interaction with porous structures. *Journal of Waterway, Port, Coastal and Ocean Engineering* (ASCE) 1999; **125**(6):322–330.
2. Hu K, Mingham CG, Causon DM. Numerical simulation of wave overtopping coastal structures using the non-linear shallow water equations. *Coastal Engineering* 2000; **41**:433–465.
3. Shiach JB, Mingham CG, Ingram DM, Bruce T. The applicability of the shallow water equations for modelling violent wave overtopping. *Coastal Engineering* 2004; **51**:1–15.
4. Stansby PK, Feng T. Surf zone wave overtopping a trapezoidal structure: 1-D modelling and PIV comparison. *Coastal Engineering* 2004; **51**:483–500.
5. Soliman A. Numerical study of irregular wave overtopping and overflow. *Ph.D. Thesis*, Nottingham University, U.K., 2003.
6. Soliman A, Reeve DE. Numerical study for small freeboard wave overtopping and overflow of sloping sea walls. *Proceedings of Coastal Structures*, Portland, U.S.A., 2003; 643–655.
7. Garcia N, Lara JL, Losada JJ. 2-D numerical analysis of near-field flow at low-crested permeable breakwaters. *Coastal Engineering* 2004; **51**:991–1020.
8. Li TQ, Troch P, Rouck JD. Wave overtopping over a sea dyke. *Journal of Computational Physics* 2004; **198**:686–726.
9. Koshizuka S, Tamako H, Oka Y. A particle method for incompressible viscous flow with fluid fragmentation. *Journal of Computational Fluid Dynamics* 1995; **4**:29–46.



10. Hayashi M, Gotoh H, Memita T, Sakai T. Gridless numerical analysis of wave breaking and overtopping at upright seawall. *Proceedings of 27th International Conference on Coastal Engineering*, Sydney, Australia, 16–21 July 2000; 2100–2113.
11. Lucy LB. A numerical approach to the testing of the fission hypothesis. *Astronomical Journal* 1977; **82**(12): 1013–1024.
12. Monaghan JJ. Smoothed particle hydrodynamics. *Annual Review of Astronomy and Astrophysics* 1992; **30**:543–574.
13. Gomez-Gesteira M, Cerqueiro D, Crespo C, Dalrymple RA. Green water overtopping analyzed with a SPH model. *Ocean Engineering* 2005; **32**:223–238.
14. Shao SD, Lo EYM. Incompressible SPH method for simulating Newtonian and non-Newtonian flows with a free surface. *Advances in Water Resources* 2003; **26**(7):787–800.
15. Cummins SJ, Rudman M. An SPH projection method. *Journal of Computational Physics* 1999; **152**:584–607.
16. Lin PZ, Liu PLF. A numerical study of breaking waves in the surf zone. *Journal of Fluid Mechanics* 1998; **359**:239–264.
17. Bradford SF. Numerical simulation of surf zone dynamics. *Journal of Waterway, Port, Coastal and Ocean Engineering* (ASCE) 2000; **126**(1):1–13.
18. Monaghan JJ. SPH compressible turbulence. *Monthly Notices of the Royal Astronomical Society* 2002; **335**: 843–852.
19. Violeau D, Piccon S, Chabard JP. Two attempts of turbulence modeling in smoothed particle hydrodynamics. *Proceedings of 8th International Symposium on Flow Modeling and Turbulence Measurements*, Tokyo, Japan, 4–6 December 2001.
20. Shao SD, Gotoh H. Turbulence particle models for tracking free surfaces. *Journal of Hydraulic Research* 2005; **43**(3):276–289.
21. Gotoh H, Shibahara T, Sakai T. Sub-particle-scale turbulence model for the MPS method—Lagrangian flow model for hydraulic engineering. *Journal of Computational Fluid Dynamics* 2001; **9**(4):339–347.
22. Shao SD. Simulation of breaking wave by SPH method coupled with  $k-\epsilon$  model. *Journal of Hydraulic Research* 2005, in press.
23. Rodi W. *Turbulence Models and Their Application in Hydraulics—A State-of-the-Art Review*. IAHR Publication, 2000.